Atmos. Chem. Phys. Discuss., 11, 27285–27325, 2011
www.atmos-chem-phys-discuss.net/11/27285/2011/
doi:10.5194/acpd-11-27285-2011

Atmospheric Chemistry and Physics Discussions

The mineral dust cycle in EMAC 2.40: sensitivity to the spectral resolution and the dust emission scheme

G. Gläser[1], **A. Kerkweg**[1], **and H. Wernli**[2]

[1]Institute for Atmospheric Physics, University of Mainz, 55099 Mainz, Germany
[2]Institute for Atmospheric and Climate Science, ETH Zurich, Zurich, Switzerland

Received: 22 June 2011 – Accepted: 26 September 2011 – Published: 5 October 2011

Correspondence to: G. Gläser (glaeseg@uni-mainz.de)

Published by Copernicus Publications on behalf of the European Geosciences Union.

Abstract

This first detailed analysis of the mineral dust cycle in the ECHAM5/MESSy Atmospheric Chemistry (EMAC) model system investigates the performance of two dust emission schemes, following the approach of Balkanski et al. (2004) and Tegen et al. (2002), respectively, and the influence of the horizontal model resolution. Here the spectral resolutions T42, T63, T85, and T106 are investigated. A basic sulphur chemistry, enabling the coating of insoluble dust particles to make them soluble, is employed in order to realistically describe the scavenging and wet deposition of mineral dust. Independent of the dust emission scheme the five-year simulations with the horizontal resolutions T42 and T63 produce unrealistically high emissions at some grid points in the Tarim Basin in Central Asia, leading to very high dust loads in polar regions. In these coarse resolutions dust source grid points in the basin and elevated grid points of the Himalayas with high wind speeds can not be distinguished, causing this overestimation. In T85 and T106 these regions are well separated and considerably less dust is emitted there. With the chosen model setup, the dust emission scheme by Balkanski et al. (2004) places the global maximum of emissions in the Thar Desert in India. This is unrealistic as the Sahara Desert is known to be the largest dust source in the world. This is the main deficiency of this scheme compared to the one by Tegen et al. (2002), which produces very reasonable distributed emissions and dust loads in simulations with resolutions T85 and T106. For future climate simulations with EMAC that focus on mineral dust, we recommend to use the dust emission scheme by Tegen et al. (2002) and a model resolution of at least T85. Simulations of two selected episodes and comparison to observational data sets show that in this model configuration EMAC is able to realistically simulate also intense, episodic events of dust emission and long-range transport.

ACPD

11, 27285–27325, 2011

1 Introduction

Airborne mineral dust particles have the potential to influence regional and global climate. Dust aerosol directly changes the radiation budget by scattering and absorption (Haywood et al., 2001; DeMott et al., 2003b). Dust particles also act very efficiently as ice nuclei (IN) causing indirect radiative effects by impacting ice clouds (Zuberi et al., 2002; DeMott et al., 2003a,b; Sassen et al., 2003). However, there are still huge uncertainties about the magnitude of these direct and indirect effects on the global climate (IPCC, 2007).

Furthermore, mineral dust influences oceans and rain forests by providing nutrients as iron and phosphorous to these ecosystems (Martin and Fitzwater, 1988; Swap et al., 1992; Chadwick et al., 1999). Moreover, dust particles can have negative impacts on human health (Kwon et al., 2002; Chen et al., 2004).

Due to uncertainties in the source and sink processes of the mineral dust cycle, Global Chemistry Climate Models (GCCMs) cover a very wide range of values for the global dust emission and deposition, the total dust burden and its life time. In the AEROCOM project (http://nansen.ipsl.jussieu.fr/AEROCOM/) the results of several GCCMs have been compared with each other and with observations. Models simulate global dust emissions between 514 and 4313 Tg yr^{-1} and dust loads ranging from 6.8 to 29.5 Tg (Textor et al., 2006; Huneeus et al., 2011).

This study is the first detailed analysis and evaluation of the mineral dust cycle in the ECHAM5/MESSy Atmospheric Chemistry (EMAC) GCCM (http://www.messy-interface.org). It is known that Global Circulation Models (GCMs) can produce considerably different results depending on the model resolution. For instance, there are differences in the simulation of extratropical cyclones with the ECMWF model at various resolutions (Jung et al., 2006), and of storm-tracks, characteristics of the NAO and inter-annual variability in the tropics with the "Institut Pierre Simon Laplace (IPSL) coupled ocean-atmosphere GCM" (Marti et al., 2010), and in the simulation of relative humidity and aerosol optical thickness with the GMI CTM (Bian et al., 2009). Therefore, we investi-

ACPD
11, 27285–27325, 2011

gate the impact of the horizontal resolution on the dust cycle. For this, five-year time slice simulations with four different resolutions (T42 ≈2.8°, T63 ≈1.9°, T85 ≈1.4°, and T106 ≈1.1°) are considered in this study. The time slices are driven by constant boundary conditions, e.g. monthly values of the sea surface temperature and the emissions of chemical species, to enable the calculation of climatological means.

We also analyse the impact of the dust emission scheme because this plays a decisive role for the simulation of the entire dust cycle (Kang et al., 2011). For each of the four model resolutions, simulations with two different emission schemes are conducted, namely, the schemes described in Balkanski et al. (2004) and in Tegen et al. (2002).

In addition to the climatological analyses the ability of EMAC to reproduce single dust outbreaks is studied. With the most reasonable model setup, with regard to climatological aspects, two episodes are simulated and compared with observational data sets. The first episode in May and June 2006 coincides with the SAMUM field campaign in southern Morocco (Kandler et al., 2009). Hence, we compare our simulation to the measured dust concentration provided by SAMUM. The second episode covers a dust outbreak from the Sahara to Central Europe in May and June 2008. The dust plume is apparent in measurements of the IN concentration at Mt. Kleiner Feldberg in Germany (Klein et al., 2010), which are compared with the model results.

In Sect. 2 we describe the GCCM EMAC including the different setups used for this work and various data sets for the comparison with the simulations. The analysis of the five-year time slice simulations is presented and discussed in Sect. 3.1. The most appropriate setup is analysed in more detail in Sect. 3.2, followed by the investigation of the two single dust episodes in Sect. 4. Section 5 contains a summary and conclusions.

ACPD
11, 27285–27325, 2011

2 Model and data

2.1 The Global Chemistry Climate Model EMAC

The GCCM EMAC couples the 5th generation European Centre Hamburg GCM (ECHAM5) (Röckner et al., 2006) to the Modular Earth Submodel System (MESSy) (Jöckel et al., 2005, 2010). In EMAC the emission, the deposition and ageing processes of aerosols are calculated in the following submodels: online emissions (ONLEM, Kerkweg et al., 2006b), scavenging (SCAV, Tost et al., 2006), sedimentation (SEDI) and dry deposition (DRYDEP, Kerkweg et al., 2006a). For this study we used the microphysical aerosol model M7 (Vignati et al., 2004), implemented as described by Kerkweg et al. (2008). M7 describes the aerosol distribution by four soluble and three insoluble log-normal modes. Freshly emitted dust particles are assumed to be always insoluble and can belong to the accumulation and the coarse mode. They become soluble either by intermodal coagulation or due to the condensation of sulphuric acid. Wet deposition is the most important removal process for dust. Soluble particles are scavenged more efficiently than insoluble ones. Hence, a reasonable sulphur chemistry is required to move dust particles from the insoluble modes to the respective soluble mode. Gas phase chemistry is simulated by MECCA (Module Efficiently Calculating the Chemistry of the Atmosphere, Sander et al., 2011). A simulation with T42 resolution without any sulphurous species produced an unrealistic, almost homogeneous global dust distribution. Further tests indicated that not the most complex, and therefore computationally most expensive, chemistry setup is needed to simulate a reasonable global dust distribution. The minimum requirements in terms of chemistry are to include basic sulphur chemistry in order to correctly represent the ageing processes of the dust particles. The chosen chemistry setup contains 44 gas phase and 13 photolysis reactions including HO_x, NO_x, and sulphur chemistry. The full chemical mechanism is listed in the electronic Supplement: "The Basic Sulphur Chemical Mechanism of MECCA".

ACPD
11, 27285–27325, 2011

The entire dust cycle in the model crucially depends on the dust emission scheme. The default emission scheme in EMAC is described in Balkanski et al. (2004). Besides the Balkanski scheme (BK from now on) a second dust emission scheme has been implemented for this study to quantify the effect of the emission scheme. As second scheme the one by Tegen et al. (2002), in the following referred to as TG, was chosen. Both, BK and TG calculate the dust emission online in every time step, i.e., in response to prognostic model variables. BK requires three external input fields: threshold 10-m wind velocity (v_{thr}), source strength factor (SSF), and clay content. No dust particles are emitted if the soil is too wet. The clay content is used to calculate the drying rate of the soil as a function of recent precipitation and surface temperature, as clay retains water for a longer time than other soil types. Hence, the higher the clay content, the longer the surface soil needs to dry. For each desert grid point, where the soil is dry enough, the vertical dust emission flux (VDEF) is calculated as a function of v_{thr}, SSF and, the 10-m wind velocity ($v_{10\text{-m}}$) according to:

$$\mathrm{VDEF} = \mathrm{SSF} \cdot (v_{10-\mathrm{m}} - v_{\mathrm{thr}}) \cdot (v_{10-\mathrm{m}})^2 .$$

The emitted dust aerosol is described as a log-normal size distribution with a mass mean radius (mmr) of 1.25 µm and a standard deviation (σ) of 2 µm.

The scheme of Tegen is much more complex (see Tegen et al. (2002), Stier et al. (2005), and Cheng et al. (2008) for details): In return, it provides more information about the dust emission, which is calculated from 192 internal dust size classes i ranging from 0.2 to 1300 µm in diameter. For each class an individual threshold friction velocity ($u_{*\mathrm{thr}}(i)$) is specified. The soil of each dust source grid box consists of a varying portion of four soil types: clay, silt, medium/fine sand, and coarse sand. In addition, preferential source regions (dried paleolake beds) are prescribed that are particulary active for 10-m wind speeds above 10 m s^{-1}. From these soil texture classes, required as input fields, the relative surface area covered by each dust size class i (s_i) is com-

ACPD
11, 27285–27325, 2011

puted. The horizontal particle flux (HPF) is then calculated for each i as follows:

$$\mathrm{HPF}(i) = \frac{\rho_a}{g} \cdot u_*^3 \cdot \left(1 + \frac{u_{*\mathrm{thr}}(i)}{u_*}\right) \cdot \left(1 - \frac{u_{*\mathrm{thr}}^2(i)}{u_*^2}\right) \cdot s_i$$

if $u_* \geq u_{*\mathrm{thr}}(i)$, $(\mathrm{HPF}(i) = 0$, otherwise$)$,

with ρ_a the air density, g the gravitational constant, and u_* the surface wind stress that is calculated from the prognostic 10-m wind speed. The horizontal fluxes are turned into the respective vertical dust emission fluxes VDEF by:

$$\mathrm{VDEF}(i) = \alpha \cdot f(\mathrm{LAI}) \cdot \mathrm{HPF}(i) \cdot I_\Theta,$$

where α describes the soil texture characteristics. For the Leaf Area Index (LAI) monthly mean values are prescribed. The LAI-dependent function takes into account that the flux increases or decreases depending on the vegetation. I_Θ is 0 if the ratio of prognostic soil moisture to the field capacity is higher than 0.99 and 1 otherwise (Tegen et al., 2002). The vertical emission fluxes of the single size classes are summed up to get a bimodal dust emission with an insoluble accumulation mode (mmr = 0.37 µm, σ = 1.59 µm) and an insoluble coarse mode (mmr = 1.75 µm, σ = 2 µm) (Cheng et al., 2008).

As an example the values of the input fields of two prominent dust source regions, the Bodélé Depression in Chad and the Thar Desert in North-West-India, are shown in Table 1. With BK 10-m wind speeds of more than 7.2 m s^{-1} are necessary to mobilise particles from the Bodélé Depression while only 6 m s^{-1} are required in the Thar Desert. The SSF is about 3.5 times higher in Thar than in Bodélé. The LAI for TG varies from 0.27 to 0.43 over the year in the Thar Desert where the soil consists mainly of medium-fine and fine particles. In the Bodélé Depression LAI is constantly 0 and the particles are assumed to be in the coarse texture class.

How these two very different schemes behave dependent on the region and the 10-m wind speed is shown in Fig. 1. For this example the soil wetness is set to 0. The two

ACPD
11, 27285–27325, 2011

schemes produce similar fluxes in the Bodélé Depression for 10-m wind speeds up to 10 m s^{-1}. Higher velocities cause higher emissions with TG because the Bodélé Depression is a classic example of a paleolake preferential dust source area (Tegen et al., 2002). The differences in the Thar Desert are enormous. The relatively low v_{thr} and the high SSF cause very strong emissions with BK.

2.2 Comparison datasets

To validate the EMAC simulations of two episodes in Sect. 4 we used the following in situ measurements, numerical model products, and satellite images.

2.2.1 The Saharan Mineral Dust Experiment SAMUM

During the SAMUM 2006 field campaign physical and chemical properties of desert aerosols were measured in southern Morocco near Tinfou (30°14′ N, 5°36′ W, 684 m a.s.l.) (Kandler et al., 2009; Knippertz et al., 2009). In Sect. 4.1 the measured concentrations of the total suspended particle matter (TSP) and of particles smaller than 10 µm (PM_{10}) are compared to the simulated dust concentration for the entire measurement period from 12 May to 6 June 2006.

2.2.2 Measurements at Mt. Kleiner Feldberg, Germany

The number concentration of ice nuclei (IN) and PM_{10} concentrations were measured since April 2008 at the Taunus Observatory of the Goethe-University of Frankfurt/Main on Mt. Kleiner Feldberg in Germany (50°13′ N, 8°27′ E, 825 m a.s.l.) (Klein et al., 2010). In Sect. 4.2 we compare the measurements with the simulated dust concentration for the period from 23 May to 4 June 2008, which contains the strongest event of Saharan dust advection to Germany since five years (Klein et al., 2010).

ACPD
11, 27285–27325, 2011

2.2.3 Satellite (MSG) dust RGB composite

Particular combinations of different channels of the Meteosat Second Generation (MSG) satellite allow for the visualisation of single atmospheric compounds. The red-green-blue (RGB) composite of the SEVIRI (Spinning Enhanced Visible and InfraRed Imager) IR8.7, IR10.8, and IR12.0 channels shows dust aerosol in magenta colours. More information about the MSG dust RGB composite can be found in the online documentation (http://oiswww.eumetsat.org/SDDI/html/doc/dust_interpretation.pdf, 22 June 2011). These images are used to evaluate the EMAC simulation of the SAMUM episode.

2.2.4 The regional dust model BSC/DREAM8b

Additionally, short-range forecasts of the Dust REgional Atmospheric Model (DREAM) are used for validation of the episodes. DREAM simulates the atmospheric dust cycle with the emission scheme of Shao and Raupach (1993) modified by Janjic (1994) and Fecan et al. (1999). The model version 8b has a horizontal resolution of 50 x 50 km and 24 layers extending up to 15 km. For further deteils see Nickovic et al. (2001), Perez et al. (2006a,b), and http://www.bsc.es/plantillaH.php?cat_id=322, 22 June 2011.

3 Five-year time slice simulations with EMAC

For the sensitivity study the model is used in the free running mode. No "nudging" towards realistic meteorology is applied because it is planned to compare the results of the simulations in the recent climate with those in earlier climate epochs for which no analysis data are available.

ACPD
11, 27285–27325, 2011

3.1 Sensitivity of the dust cycle to model resolution and the dust emission scheme

In this section, the entire dust cycle is analysed with respect to the horizontal model resolution and the dust emission scheme. The aim is to determine the model setup that produces the most reasonable mineral dust cycle.

Table 2 shows the five-year means of the global dust emissions, load, life time, and wet deposition as simulated by EMAC using T42≈2.8°, T63≈1.9°, T85≈1.4°, and T106≈1.1° spectral resolutions. For each resolution the results with the two emission schemes BK and TG are listed. The total dust deposition does not deviate more than 2 % from the emissions and there is no trend in the dust load over the five years showing that the dust budget is closed. The life time is calculated as the ratio of dust load to total dust deposition. With the eight different setups, the emissions range from 1651 to 3238 Tg yr^{-1}, the load from 22.18 to 36.20 Tg and the life time from 3.98 to 6.19 days. We first note that all the values of the dust emission and life time are within the very wide range of earlier estimates based upon model simulations (AEROCOM: Textor et al., 2006; Huneeus et al., 2011). The dust load, however, exceeds this range in the T63BK, T85BK, T106BK, and T106TG simulations. The global distribution of dust emissions and loads of the eight experiments are illustrated in Figs. 2 and 3, respectively. At first sight, each setup produces reasonable distributions. A closer look at single regions reveals interesting differences. Independent of the model resolution BK simulates the global maximum of the emissions in North-West-India, leading to the global maximum in the loads in the same region (left panels in Figs. 2 and 3). For the same location emissions of the TG scheme are in general much lower and comparable to the values at other hotspots like the Bodélé Depression in Chad (right panels in Figs. 2 and 3). According to other studies, the Sahara is the major dust source in the world (Prospero et al., 2002; Washington et al., 2003; Ginoux et al., 2004). The averaged dust emission of the four simulations with BK accounts for 608 Tg yr^{-1} in the Sahara (5°–36° N, 20° W–40° E) and 1483 Tg yr^{-1} in India (20°–33° N, 65°–85° E). This

ACPD
11, 27285–27325, 2011

means, that the dust emissions in India are 2.4 times higher than in the Sahara, which is in clear contradiction to published values. TG on average simulates 925 Tg yr^{-1} in the Sahara and 169 Tg yr^{-1} in India. The results for the Sahara dust emissions are inside the wide span of published values for each of the time slices (Washington et al., 2003; Ginoux et al., 2004; Huneeus et al., 2011). Very strong emissions in India with BK result from a relatively low 10-m wind speed threshold and a pretty high source strength factor in this region compared to values in the Sahara (see Sect. 2.1, in particular the discussion of Fig. 1). In other regions of the world the differences between BK and TG are relatively small. Due to the strong overestimation of emissions in India with BK the TG scheme is overall regarded as the more reliable dust emission scheme for the EMAC model at resolutions between T42 and T106.

Besides the differences in the global mean values (see Table 2) the model resolution influences the patterns of the dust emissions and loads. For both emission schemes the coarser resolutions T42 and T63 generate some grid points with pretty high emissions in the area of the Taklamakan Desert in the Tarim Basin north of the Himalayas (Fig. 2a, b, e, f). The mean emission with T42 and T63 within the small box [34°–40° N, 75°–95° E] is about half of the mean emission in entire North Africa. This causes unrealistic high dust loads in polar regions of more than 10 mg m^{-2} north of 80° N (Fig. 3a, b, e, f). The mean load of all AEROCOM models is less than 5 mg m^{-2} in this region (http://dataipsl.ipsl.jussieu.fr/cgi-bin/AEROCOM/aerocom/surfobs_annualrs.pl, choose as Species: DUST and as Parameter: LOAD, 22 June 2011). The strong emissions in the Taklamakan Desert with T42 and T63 occur due to a combination of an orographic effect and the coarse resolution. At the steep northern slope of the Himalayas the model produces pretty high near-surface wind velocities at elevated grid points. Due to the coarse resolution some of these grid points are preferential dust source regions. In T85 and T106 it becomes possible to distinguish between elevated grid points with high winds and those in the basin, which are the dust source grid points. Because of these deficiencies - unrealistically high emissions in the Tarim Basin that cause too high dust loads in the Arctic - model simulations with T42 and T63 produce a less realistic global

ACPD
11, 27285–27325, 2011

dust cycle than T85 and T106.

The quantitative differences between T85 and T106 with the TG scheme are substantial: Mean dust emissions and loads are almost 50% higher in T106 than in T85. The higher emissions are caused by differences in the 10-m wind velocities at dust source grid points, where the mean wind speed is on average 3.5 % higher in T106 than in T85. The global distributions, however, look quite similar (see Figs. 2g, h and 3g, h) and appear reasonable. Hence, we cannot decide which simulation is closer to reality. Both simulations produce dust emissions and life times that are within the range of earlier estimates. Because the dust load of T106TG exceeds the range of the AEROCOM models and in terms of computational costs, the T85 setup with the TG scheme is the one to prefer, in particular for long-term climate simulations.

Some other interesting aspects are illustrated in Fig. 4, which shows relative sensitivities of variables (dx_i) with respect to the model setup:

$$dx_i = \frac{x_i - x_m}{x_m} \cdot 100. \quad (1)$$

The considered variables x are emission, load, life time, and the ratio of wet to total deposition of dust. The index i refers to the experiments T42BK, T63BK, T85BK, T106BK, T42TG, T63TG, T85TG, and T106TG and x_m to the mean over the eight simulations.

With BK, dust emissions increase and life times decrease with increasing model resolution. The dust load, however, is lower in T85BK and T106BK than in T63BK although the emissions are higher leading by definition to the shorter life times. Scavenging accounts for about 78 % of the total deposition (Table 2) and does not vary a lot between the resolutions. One possible explanation for the decreasing life times from T42 to T106 could be that the dust particles need longer to reach a precipitating cloud and thus, get scavenged later the coarser the resolution is.

With TG the life times show the same trend as with BK, the dust emissions also increase with finer resolution except in T85TG where the emission is lower than in

ACPD
11, 27285–27325, 2011

T63TG. The same is true for the dust load, which is in T85TG even lower than in T42TG.

With both emission schemes the wet-to-total deposition rate is hardly dependent on the resolution, but it is generally higher with BK than with TG.

3.2 Regional analysis of T85TG

A more detailed analysis of the T85TG simulation to assess the characteristics of the dust cycle as simulated by this model setup is provided in the following. More explicitly, the seasonal cycle of the emissions in the Thar Desert and in Central Asian dust source regions are investigated.

Figure 5 shows the seasonal variation of the dynamics and the dust cycle on the Indian subcontinent. In winter (DJF, Fig. 5a) the ITCZ lies south of the equator and the wind arrows over the Indian Ocean illustrate the north-easterly trade winds. During this season there is almost no dust activity in this region. In summer (JJA, Fig. 5b) the strong south-westerly trade winds mobilise a huge amount of dust when they make landfall in the region of the Thar Desert in the north-western part of India. The dust particles get washed out by the monsoon-related precipitation at the southern slope of the Himalayas. This effect causes the global maxima of the dust emission and deposition in this region in JJA. According to Habib et al. (2006), the TOMS-AI (Total Ozone Mapping Spectrometer-Aerosol Index) shows a similar annual cycle as the dust load of T85TG. They defined a dust-dominated region (two contiguous rectangular boxes: 28°–32° N, 62°–72° E and 24°–28° N, 62°–78° E) where the maximum of TOMS-AI is observed in June. The total dust load of soluble and insoluble particles simulated by EMAC reaches its maximum in July. The presence of clouds could obscure the aerosol detection by TOMS leading to an underestimation of the aerosol load during the monsoon period from June to September (Habib et al., 2006). This could explain the slight deviation between the observed and the simulated values.

Dust emissions from Central and East Asia show a different annual cycle (not shown here): strong spring-time winds associated with frontal cyclones cause the strongest

ACPD
11, 27285–27325, 2011

dust emissions from March to May (Tegen et al., 2002; Zhao et al., 2008; Geng et al., 2009). This spring-time maximum of Asian dust source activity is captured by T85TG. As in Laurent et al. (2006) the emissions from the Chinese and Mongolian deserts (35.5°–47° N, 73°–125° E) are by far most intense in April, followed by May and March. Consistently, the lowest values are simulated in DJF due to high soil moisture or snow cover in this season.

4 Two single dust episodes simulated with T85TG

The intensity of dust emission varies dependent on the meteorological situation. Single dust outbreaks, lasting a few days, can contribute a large amount to the annual emitted dust of a single region. This chapter investigates the ability of EMAC using the T85TG setup to reproduce such events. To compare the simulation with measurements the model was nudged to reanalysis data of the European Centre for Medium-range Weather Forecasting (ECMWF). The nudging through the Newtonian relaxation of the four prognostic model variables temperature, divergence, vorticity, and the logarithm of surface pressure is only applied in the free troposphere (Jöckel et al., 2006).

4.1 May/June 2006: SAMUM

During the Saharan Mineral Dust Experiment (SAMUM: Kandler et al., 2009; Knippertz et al., 2009) the mass concentrations of desert aerosols were measured near Tinfou (30°14′ N, 5°36′ W, 684 m a.s.l.) in southern Morocco from 12 May to 6 June 2006. For this episode the period from 1 April to 30 June 2006 was simulated.

Figure 6 compares the simulated dust concentrations of the grid box containing the measurement site with the measured ones. The diameter of the largest emitted particles in TG is 15.88 µm. The simulated mean concentration is with 407 µg m^{-3} 37% higher than the PM_{10} measurements (291 µg m^{-3}) and much lower than the TSP values (9742 µg m^{-3}). In the measurements particles larger than 10 µm in diameter account

ACPD
11, 27285–27325, 2011

for more than 90% of the total airborne aerosol mass under high dust concentrations. Local wind speed observations indicate that large particles (d >10 µm) were locally emitted, while a significant portion of the smaller ones stems from remote sources and was advected to the measurement site (Kandler et al., 2009). This explains the difference between measured and simulated concentrations, especially during the local strong-wind period from 23 to 27 May. Due to its coarse horizontal resolution of about 155 km, EMAC is not able to produce strong local dust emission events that, e.g., result from canalisation effects of the regional orography. A second reason for the differences of the concentration values during this period is that TG does not take the super-coarse mode into account. However, this mode contributes most to the observed total aerosol mass, as described above. Overall, it is a satisfying result that the mean value of the simulated dust concentration over the whole time series is higher than the measured PM_{10} and much lower than the TSP concentration.

Regional scale effects that are not captured by EMAC with the horizontal resolution T85 could lead to a time shift between measurements and the simulation. For instance, there is a measured maximum on 1 June while a peak in the simulation occurs on 2 June. Therefore, mean values for the six periods, named DP1, DP2, DP3, IP1, IP2, and "advection from SE", as described by Kandler et al. (2009) are considered, that are displayed in Fig. 6.

As described above, during DP1, IP1, and IP2 the simulated concentrations are higher than the PM_{10} and lower than the TSP measurements. The low-dust periods IP1 and IP2 illustrate desert background conditions that are represented well by EMAC. Without freshly emitted, large particles the TSP concentrations are only slightly above the simulated ones. DP2 is the local strong-wind period discussed earlier. The concentrations for the period "advection from SE" (Kandler et al., 2009) are underestimated by EMAC. This is due to relatively small discrepancies between the simulated and real flow patterns. At least the simulated concentration of soluble particles is one order of magnitude higher than the one of insoluble particles (not shown). This indicates that the dust has been advected to the measurement site because freshly emitted dust is

ACPD
11, 27285–27325, 2011

assumed to be insoluble in the model. For DP3 the simulated concentrations are even higher than TSP. The periods "advection from SE" and DP3 are further investigated and compared to satellite images and BSC/DREAM8b simulations later in this chapter.

In contrast to those longer periods, two density currents were observed during SAMUM that generated high dust concentrations on 12 and 13 May (DC1) and on 31 May and 1 June (DC2) as discussed by Knippertz et al. (2007). DC1 is apparent in EMAC by a rapid increase of the simulated concentrations of insoluble particles in the night from 12 to 13 May. The measured TSP values are one order of magnitude higher because of the mobilisation of super-coarse particles that are not emitted in the model as mentioned above. The simulated concentrations are pretty low when DC2 was observed, but they increase rapidly somewhat later. Here again regional scale canalisation effects could be the reason for a delayed arrival of dusty air at Tinfou in the model.

This analysis points out the limitations of the global model concerning the regional and temporal resolution of small-scale processes causing massive dust emission. We also note that a comparison between a global simulation and measurements at one station is problematic. However, there are only a few measurements of dust concentrations. Hence, this comparison is the only possiblity to compare measured and simulated dust concentrations directly. A more equitable approach to evaluate EMAC is to validate the results on a larger scale.

Figure 7 compares EMAC with the forecasts of the BSC/DREAM8b model and the MSG dust RGB composite at 12:00 UTC 1 June 2006. Both models simulate dust concentrations higher than 5000 $\mu g\,m^{-3}$ on the lowest model layer in central Algeria. The pinkish colours in the MSG composite corroborate a huge amount of airborne dust in this region. Also in the southern part of Mauritania there are high concentrations in the satellite image and in the EMAC results. BSC/DREAM8b shows a more uniform distribution over Mauritania and Mali with a maximum in the North of Mauritania. The biggest difference between the models is simulated over eastern Egypt, where BSC/DREAM8b produces more than 1000 $\mu g\,m^{-3}$ and EMAC less than 40 $\mu g\,m^{-3}$. The MSG composite

ACPD
11, 27285–27325, 2011

shows no indication of high dust concentrations in this region.

On several other days during this episode the MSG dust composite shows dust aerosol in single regions over North Africa (not shown). There is high qualitative congruence between the EMAC results and the satellite composites at days with strong signals in the MSG images, e.g., on 11 May in South-Algeria and Niger, on 16 May in West-Algeria, on 22 May in West-Algeria, North-Mali and North Mauritania, on 24 and 25 May in West-Algeria and Mali, and on 29 May in West-Mali and South-East-Mauritania.

The period "advection from SE" on 21 and 22 May seemed not to be captured by the model on the first sight. However, on 21 and 22 May the model simulates high dust emissions in Mali and West-Algeria. This dust is transported northwards but not far enough to reach Tinfou. The comparison to MSG composites confirms that this event is reproduced quite well. Only a small displacement inhibits a better agreement with in situ measurements in this case.

During DP3 EMAC produces a higher dust concentration than observed. Satellite images and the 2-D-fields of the simulated dust concentrations show a dust front evolving in North-Algeria on 1 June that spreads south-westwards on the following days. The MSG composites indicate a good representation of the location of the dust front by the model. However, EMAC overestimates the dust emission along the front leading to higher concentrations at the measurement station than observed. From the model results no clear distinction can be made between DC2 and the advection of air with high dust concentrations from North-Algeria.

Further insight into this episode can be obtained by trajectory analyses. Trajectories were calculated using the LAGRangian ANalysis TOol (LAGRANTO: Wernli and Davies, 1997). Here the simulated and observed peak in the dust concentrations at the SAMUM measurement site on 3 June is investigated. Eight-day backward trajectories starting from the three lowest model layers at the station show the simulated dust emission and concentration along the air parcel trajectories (Fig. 8). Strong emissions of more than 20 $\mu g\,m^{-2}\,s^{-1}$ during 1 June (even 50–100 $\mu g\,m^{-2}\,s^{-1}$ in the first hours of

ACPD
11, 27285–27325, 2011

the day) lead to a rapid increase in the dust concentrations along the trajectories. The heavy emissions can also be seen in the MSG dust composite at 12:00 UTC 1 June (Fig. 7c). This reveals that the dust reaching Tinfou on 3 June was emitted on 1 June over the southern slope of the Atlas Mountains in Algeria.

Figure 9 shows the mean values of several variables along the trajectories. The very abrupt acceleration of the 10-m wind speed during the first hours of 1 June from 6 to 9 $m\,s^{-1}$ causes strong dust emissions of about 100 $\mu g\,m^{-2}\,s^{-1}$ which again lead to an abrupt increase of the dust concentration from less than 100 to more than 4000 $\mu g\,m^{-3}$. While the 10-m wind velocity and the emissions decrease during the following two days, the concentration stays on a high level. When the air reaches the measurement site on 3 June 00:00 UTC a value of about 1700 $\mu g\,m^{-3}$ is simulated.

Figure 9 shows high 10-m wind speeds also on 27, 28, and 30 May. The maximum on 27 May is associated with high dust emissions in central Algeria (see also Fig. 8). However, during this time the altitude of the trajectories is too high for the air parcels to be direcly affected by these emissions. Therefore, the freshly emitted dust does not reach the trajectories and the dust concentration does not increase. The two peaks in the wind speed on 28 and 30 May occur when the trajectories cross the Mediterranean, where dust emission is impossible.

4.2 May/June 2008: Mt. Kleiner Feldberg

At the Taunus Observatory of the Goethe-University of Frankfurt/Main on Mt. Kleiner Feldberg in Germany (50°13′ N, 8°27′ E, 825 m a.s.l.) the number concentration of ice nuclei (IN) and PM_{10} concentrations were measured since April 2008 (Klein et al., 2010). Here, a Sahara dust episode observed in May 2008 is considered. The EMAC simulation was performed from 1 April to 30 June 2008.

The measured concentrations of PM_{10} and IN, the simulated dust concentrations of BSC/DREAM8b, and the concentrations of the grid box containing the measurement site simulated by EMAC show peaks at the end of May 2008 (Fig. 10). The mean values from 24 May to 1 June are highest in the EMAC simulation with 54.84 $\mu g\,m^{-3}$, followed

ACPD
11, 27285–27325, 2011

by BSC/DREAM8b with 43.38 µg m^{-3} and the PM_{10} measurements with 23.91 µg m^{-3}. This is a reasonable result because the maximum diameter of particles in EMAC is 15.88 µm (see Sect. 4.1) while it is 12 µm in the BSC/DREAM8b data and, self-evident, 10 µm in the PM_{10} measurements.

The absolute maximum is simulated at the same time by EMAC and BSC/DREAM8b, i.e., in the afternoon hours of 28 May. It reaches values of 218 µg m^{-3} in EMAC and 196 µg m^{-3} in the BSC/DREAM8b simulation. The PM_{10} measurements show no distinct peak at this time, but one and two days later, when the simulated values decrease again. BSC/DREAM8b reproduces the observed peaks on 29 and 30 May, while the decline in EMAC is almost monotonously. Klein et al. (2010) assumed that the deviations on 28 and 29 May can be traced back to thunderstorm development over the Taunus hills that is not represented in BSC/DREAM8b and EMAC because it is a subscale phenomenon. This could explain the much higher congruence between the two simulations compared to the one between the simulations and the PM_{10} measurements. Another effect, that might reduce the comparability of these time series, is the fact that many other species like soot, acids, and sea salt contribute to the PM_{10} measurements (Klein et al., 2010).

The correlation is higher between the simulated dust concentrations and the measured IN concentrations. Mineral dust particles act very efficiently as heterogeneous ice nuclei (Zuberi et al., 2002; DeMott et al., 2003a,b; Cziczo et al., 2004; Richardson et al., 2007). Linear regression of IN number concentration against simulated dust concentration yields correlation coefficients $R_{DREAM} = 0.888$ and $R_{EMAC} = 0.729$ for the BSC/DREAM8b and the EMAC simulation, respectively.

As before, for this episode the source region of the dust that reaches Central Europe can be identified by backward trajectories. Very strong dust emissions in Central Algeria of more than 200 µg m^{-2} s^{-1} on 26 May (Fig. 11 a) lead to high dust concentrations along the trajectories. The concentrations decrease from more than 2000 µg m^{-3} on 26 May to values of about 200 µg m^{-3} when the trajectories reach Mt. Kleiner Feldberg (Fig. 11 b). Klein et al. (2010) show backward trajectories calculated by the German

ACPD
11, 27285–27325, 2011

Meteorological Service confirming the advection of air from the Sahara to Central Europe. The EMAC results reveal that most of the dust was emitted in the afternoon of 26 May in the north-eastern part of the province Adrar in central Algeria (Fig. 11a).

In terms of source region and the direct transport pattern across the western Mediterranean, this event is comparable to the one studied by Sodemann et al. (2006) in October 2000.

5 Summary and conclusions

This study investigates the mineral dust cycle in the GCCM EMAC. In order to determine the model setup that simulates the most reasonable mineral dust cycle, sensitivity studies were conducted with regard to the chemistry setup, the horizontal model resolution, and the dust emission scheme.

Freshly emitted dust particles are assumed to be insoluble. By coating of sulphate they become soluble and are scavenged out of the atmosphere much more efficiently. Therefore, a basic sulphur chemistry is required to avoid an unrealistic, almost homogeneous distribution of the dust over the entire globe.

Results of five-year time slice simulations show in parts severe differences between the four considered horizontal resolutions (T42, T63, T85, and T106) and the two implemented dust emission schemes (by Balkanski et al., 2004 and by Tegen et al., 2002). With the resolutions T42 and T63 there are some grid points at the northern slope the Himalayas where on the one hand, high 10-m wind velocities are simulated because of high elevation, and on the other hand, these grid points belong to the Tarim Basin, which is a dust source region. Hence, T42 and T63 overestimate the dust emissions in this region. The northward transport of this dust causes unrealistically high dust loads in the Arctic. With the resolutions T85 and T106 the elevated grid points and those in the basin can be distinguished leading to much lower emissions in the Tarim Basin and a more realistic dust burden in polar regions. This behaviour is independent of the dust emission scheme.

ACPD
11, 27285–27325, 2011

Independent of the model resolution the BK scheme produces too strong emissions in the Thar Desert in North-West-India. On average the emissions are 2.4 times higher in India than in the Sahara, which is in contradiction to current scientific knowledge, considering the Sahara Desert to be the world's largest dust source.

Despite the conspicuous differences between T85 and T106 with the TG scheme, no clear statement can be made about which setup is closer to reality. More detailed analyses of the T85TG simulation show that known regional and seasonal characteristics of the dust cycle, like the monsoon-caused summer maximum in India and the spring-time maximum in Central Asia, are captured with this model setup. It is also able to simulate single dust episodes. The large scale flow patterns are reproduced and the TG scheme generates dust emissions that lead to dust concentrations in the same order of magnitude as observed. Especially the transport pathways of dust are simulated realistically according to MSG images and results of the BSC/DREAM8b. Nevertheless, the investigation of episodes points out the restrictions of the GCCM EMAC, concerning the resolution effects on small spacial and temporal scales. However, a GCCM is in general not able to resolve such small scale processes. Within the scope of a GCCM the results are absolutely satisfying. Beyond that, trajectory analyses allow for a detailed investigation of the dust transport and of the processes that occur along the pathway. For both episodes the source regions of the dust, reaching the measurement sites, could be identified.

A model setup with a horizontal resolution of T85 or finer, including a basic sulphur chemistry and using the dust emission scheme by Tegen et al. (2002) is recommended for future investigations of the mineral dust cycle with the EMAC GCCM.

Supplementary material related to this article is available online at: http://www.atmos-chem-phys-discuss.net/11/27285/2011/acpd-11-27285-2011-supplement.pdf.

ACPD
11, 27285–27325, 2011

Acknowledgements. This work was funded by the Earth System Research Centre Geocycles at the University of Mainz. We thank Rolf Sander for developing the chemistry setup and Patrick Jöckel for providing data and the introduction to EMAC. We are grateful to Peter Knippertz for helpful discussions and would like to thank Konrad Kandler for providing data of the SAMUM field campaign and Holger Klein for supplying data from Mt. Kleiner Feldberg. We thank Ina Tegen for providing the code and input fields for the TG scheme and the useful discussion about it. We used images from the BSC/DREAM8b model, operated by the Barcelona Supercomputing Center (http://www.bsc.es/projects/earthscience/DREAM/) and from the EUMETSAT MSG 0° satellite. The simulations were performed at the German Climate Computing Center (DKRZ) in Hamburg.

References

Balkanski, Y., Schulz, M., Claquin, T., Moulin, C., and Ginoux, P.: Emission of Atmospheric Trace Compounds, chap. Global Emissions of Mineral Aerosol: Formulation and Validation using satellite Imagery, 239–267, Kluwer, 2004. 27286, 27288, 27290, 27304, 27313, 27315, 27316, 27317

Bian, H., Chin, M., Rodriguez, J. M., Yu, H., Penner, J. E., and Strahan, S.: Sensitivity of aerosol optical thickness and aerosol direct radiative effect to relative humidity, Atmos. Chem. Phys., 9, 2375–2386, doi:10.5194/acp-9-2375-2009, 2009. 27287

Chadwick, O. A., Derry, L. A., Vitousek, P. M., Huebert, B. J., and Hedin, L. O.: Changing sources of nutrients during four million years of ecosystem development, Nature, 397, 491–497, 1999. 27287

Chen, Y. S., Sheen, P. C., Chen, E. R., Liu, Y. K., Wu, T. N., and Yang, C. Y.: Effects of Asian dust storm events on daily mortality in Taipei, Taiwan, Environ. Res., 95, 151–155, doi:10.1016/j.envres.2003.08.008, 2004. 27287

Cheng, T., Peng, Y., Feichter, J., and Tegen, I.: An improvement on the dust emission scheme in the global aerosol-climate model ECHAM5-HAM, Atmos. Chem. Phys., 8, 1105–1117, doi:10.5194/acp-8-1105-2008, 2008. 27290, 27291

Cziczo, D. J., Murphy, D. M., Hudson, P. K., and Thomson, D. S.: Single particle measurements of the chemical composition of cirrus ice residue during CRYSTAL-FACE, J. Geophys. Res.-Atmos., 109, D04201, doi:10.1029/2003JD004032, 2004. 27303

ACPD

11, 27285–27325, 2011

DeMott, P. J., Cziczo, D. J., Prenni, A. J., Murphy, D. M., Kreidenweis, S. M., Thomson, D. S., Borys, R., and Rogers, D. C.: Measurements of the concentration and composition of nuclei for cirrus formation, Proc. Natl. Acad. Sci. USA, 100, 14655–14660, doi:10.1073/pnas.2532677100, 2003a. 27287, 27303

DeMott, P. J., Sassen, K., Poellot, M. R., Baumgardner, D., Rogers, D. C., Brooks, S. D., Prenni, A. J., and Kreidenweis, S. M.: African dust aerosols as atmospheric ice nuclei, Geophys. Res. Lett., 30, 1732, doi:10.1029/2003GL017410, 2003b. 27287, 27303

Fecan, F., Marticorena, B., and Bergametti, G.: Parametrization of the increase of the aeolian erosion threshold wind friction velocity due to soil moisture for arid and semi-arid areas, Ann. Geophys., 17, 149–157, doi:10.5194/angeo-17-149-1999, 1999. 27293

Geng, H., Park, Y., Hwang, H., Kang, S., and Ro, C. U.: Elevated nitrogen-containing particles observed in Asian dust aerosol samples collected at the marine boundary layer of the Bohai Sea and the Yellow Sea, Atmos. Chem. Phys., 9, 6933–6947, doi:10.5194/acp-9-6933-2009, 2009. 27298

Ginoux, P., Prospero, J. M., Torres, O., and Chin, M.: Long-term simulation of global dust distribution with the GOCART model: correlation with North Atlantic Oscillation, Environ. Modell. Softw., 19, 113–128, doi:10.1016/S1364-8152(03)00114-2, 2004. 27294, 27295

Habib, G., Venkataraman, C., Chiapello, I., Ramachandran, S., Boucher, O., and Reddy, M. S.: Seasonal and interannual variability in absorbing aerosols over India derived from TOMS: Relationship to regional meteorology and emissions, Atmos. Environ., 40, 1909–1921, doi:10.1016/j.atmosenv.2005.07.077, 2006. 27297

Haywood, J. M., Francis, P. N., Glew, M. D., and Taylor, J. P.: Optical properties and direct radiative effect of Saharan dust: A case study of two Saharan dust outbreaks using aircraft data, J. Geophys. Res.-Atmos., 106, 18417–18430, 2001. 27287

Huneeus, N., Schulz, M., Balkanski, Y., Griesfeller, J., Prospero, J., Kinne, S., Bauer, S., Boucher, O., Chin, M., Dentener, F., Diehl, T., Easter, R., Fillmore, D., Ghan, S., Ginoux, P., Grini, A., Horowitz, L., Koch, D., Krol, M. C., Landing, W., Liu, X., Mahowald, N., Miller, R., Morcrette, J. J., Myhre, G., Penner, J., Perlwitz, J., Stier, P., Takemura, T., and Zender, C. S.: Global dust model intercomparison in AeroCom phase I, Atmos. Chem. Phys., 11, 7781–7816, doi:10.5194/acp-11-7781-2011, 2011. 27287, 27294, 27295

IPCC: Climate Change 2007: The Physical Science Basis. Contribution of Working Group I to the Fourth Assessment Report of the Intergovernmental Panel on Climate Change, edited by: Solomon, S., Qin, D., Manning, M., Chen, Z., Marquis, M., Averyt, K. B., Tignor, M. and

ACPD
11, 27285–27325, 2011

Miller, H. L., Cambridge University Press, Cambridge, UK and New York, NY, USA, 2007. 27287

Janjic, Z. I.: The Step-Mountain Eta Coordinate Model: Further Developments of the Convection, Viscous Sublayer, and Turbulence Closure Schemes, Mon. Weather Rev., 122, 927–945, 1994. 27293

Jöckel, P., Sander, R., Kerkweg, A., Tost, H., and Lelieveld, J.: Technical note: The Modular Earth Submodel System (MESSy) - a new approach towards Earth System Modeling, Atmos. Chem. Phys., 5, 433–444, doi:10.5194/acp-5-433-2005, 2005. 27289

Jöckel, P., Tost, H., Pozzer, A., Bruehl, C., Buchholz, J., Ganzeveld, L., Hoor, P., Kerkweg, A., Lawrence, M. G., Sander, R., Steil, B., Stiller, G., Tanarhte, M., Taraborrelli, D., Van Aardenne, J., and Lelieveld, J.: The atmospheric chemistry general circulation model ECHAM5/MESSy1: consistent simulation of ozone from the surface to the mesosphere, Atmos. Chem. Phys., 6, 5067–5104, doi:10.5194/acp-6-5067-2006, 2006. 27298

Jöckel, P., Kerkweg, A., Pozzer, A., Sander, R., Tost, H., Riede, H., Baumgaertner, A., Gromov, S., and Kern, B.: Development cycle 2 of the Modular Earth Submodel System (MESSy2), Geosci. Model Dev., 3, 717–752, doi:10.5194/gmd-3-717-2010, 2010. 27289

Jung, T., Gulev, S. K., Rudeva, I., and Soloviov, V.: Sensitivity of extratropical cyclone characteristics to horizontal resolution in the ECMWF model, Q. J. Roy. Meteorol. Soc., 132, 1839–1857, doi:10.1256/qj.05.212, 2006. 27287

Kandler, K., Schuetz, L., Deutscher, C., Ebert, M., Hofmann, H., Jaeckel, S., Jaenicke, R., Knippertz, P., Lieke, K., Massling, A., Petzold, A., Schladitz, A., Weinzierl, B., Wiedensohler, A., Zorn, S., and Weinbruch, S.: Size distribution, mass concentration, chemical and mineralogical composition and derived optical parameters of the boundary layer aerosol at Tinfou, Morocco, during SAMUM 2006, Tellus B-Chem. Phys. Meteorol., 61, 32–50, doi:10.1111/j.1600-0889.2008.00385.x, 2009. 27288, 27292, 27298, 27299, 27320

Kang, J.-Y., Yoon, S.-C., Shao, Y., and Kim, S.-W.: Comparison of vertical dust flux by implementing three dust emission schemes in WRF/Chem, J. Geophys. Res.-Atmos., 116, D09202, doi:10.1029/2010JD014649, 2011. 27288

Kerkweg, A., Buchholz, J., Ganzeveld, L., Pozzer, A., Tost, H., and Joeckel, P.: Technical note: An implementation of the dry removal processes DRY DEPosition and SEDImentation in the modular earth submodel system (MESSy), Atmos. Chem. Phys., 6, 4617–4632, doi:10.5194/acp-6-4617-2006, 2006a. 27289

Kerkweg, A., Sander, R., Tost, H., and Joeckel, P.: Technical note: Implementation of pre-

ACPD
11, 27285–27325, 2011

scribed (OFFLEM), calculated (ONLEM), and pseudo-emissions (TNUDGE) of chemical species in the Modular Earth Submodel System (MESSy), Atmos. Chem. Phys., 6, 3603–3609, doi:10.5194/acp-6-3603-2006, 2006b. 27289

Kerkweg, A., Joeckel, P., Pozzer, A., Tost, H., Sander, R., Schulz, M., Stier, P., Vignati, E., Wilson, J., and Lelieveld, J.: Consistent simulation of bromine chemistry from the marine boundary layer to the stratosphere – Part 1: Model description, sea salt aerosols and pH, Atmos. Chem. Phys., 8, 5899–5917, doi:10.5194/acp-8-5899-2008, 2008. 27289

Klein, H., Nickovic, S., Haunold, W., Bundke, U., Nillius, B., Ebert, M., Weinbruch, S., Schuetz, L., Levin, Z., Barrie, L. A., and Bingemer, H.: Saharan dust and ice nuclei over Central Europe, Atmos. Chem. Phys., 10, 10211–10221, doi:10.5194/acp-10-10211-2010, 2010. 27288, 27292, 27303, 27324

Knippertz, P., Deutscher, C., Kandler, K., Mueller, T., Schulz, O., and Schuetz, L.: Dust mobilization due to density currents in the Atlas region: Observations from the Saharan Mineral Dust Experiment 2006 field campaign, J. Geophys. Res.-Atmos., 112, doi:10.1029/2007JD008774, 2007. 27300

Knippertz, P., Ansmann, A., Althausen, D., Mueller, D., Tesche, M., Bierwirth, E., Dinter, T., Mueller, T., Von Hoyningen-Huene, W., Schepanski, K., Wendisch, M., Heinold, B., Kandler, K., Petzold, A., Schuetz, L., and Tegen, I.: Dust mobilization and transport in the northern Sahara during SAMUM 2006 - a meteorological overview, Tellus B-Chem. Phys. Meteorol., 61, 12–31, doi:10.1111/j.1600-0889.2008.00380.x, 2009. 27292, 27298

Kwon, H. J., Cho, S. H., Chun, Y., Lagarde, F., and Pershagen, G.: Effects of the Asian dust events on daily mortality in Seoul, Korea, Environ. Res., 90, 1–5, doi:10.1006/enrs.2002.4377, 2002. 27287

Laurent, B., Marticorena, B., Bergametti, G., and Mei, F.: Modeling mineral dust emissions from Chinese and Mongolian deserts, Glob. Planet. Change, 52, 121–141, doi:10.1016/j.gloplacha.2006.02.012, 2006. 27298

Marti, O., Braconnot, P., Dufresne, J. L., Bellier, J., Benshila, R., Bony, S., Brockmann, P., Cadule, P., Caubel, A., Codron, F., de Noblet, N., Denvil, S., Fairhead, L., Fichefet, T., Foujols, M. A., Friedlingstein, P., Goosse, H., Grandpeix, J. Y., Guilyardi, E., Hourdin, F., Idelkadi, A., Kageyama, M., Krinner, G., Levy, C., Madec, G., Mignot, J., Musat, I., Swingedouw, D., and Talandier, C.: Key features of the IPSL ocean atmosphere model and its sensitivity to atmospheric resolution, Clim. Dynam., 34, 1–26, doi:10.1007/s00382-009-0640-6, 2010. 27287

ACPD
11, 27285–27325, 2011

Martin, J. H. and Fitzwater, S. E.: Iron deficiency limits phytoplankton growth in the north-east Pacific subarctic, Nature, 331, 341–343, 1988. 27287
Nickovic, S., Kallos, G., Papadopoulos, A., and Kakaliagou, O.: A model for prediction of desert dust cycle in the atmosphere, J. Geophys. Res.-Atmos., 106, 18113–18129, 2001. 27293
Perez, C., Nickovic, S., Baldasano, J. M., Sicard, M., Rocadenbosch, F., and Cachorro, V. E.: A long Saharan dust event over the western Mediterranean: Lidar, Sun photometer observations, and regional dust modeling, J. Geophys. Res.-Atmos., 111, D15214, doi:10.1029/2005JD006579, 2006a. 27293
Perez, C., Nickovic, S., Pejanovic, G., Baldasano, J. M., and Oezsoy, E.: Interactive dust-radiation modeling: A step to improve weather forecasts, J. Geophys. Res.-Atmos., 111, D16206, doi:10.1029/2005JD006717, 2006b. 27293
Prospero, J. M., Ginoux, P., Torres, O., Nicholson, S. E., and Gill, T. E.: Environmental characterization of global sources of atmospheric soil dust identified with the Nimbus 7 Total Ozone Mapping Spectrometer (TOMS) absorbing aerosol product, Rev. Geophys., 40, 1002, doi:10.1029/2000RG000095, 2002. 27294
Richardson, M. S., DeMott, P. J., Kreidenweis, S. M., Cziczo, D. J., Dunlea, E. J., Jimenez, J. L., Thomson, D. S., Ashbaugh, L. L., Borys, R. D., Westphal, D. L., Casuccio, G. S., and Lersch, T. L.: Measurements of heterogeneous ice nuclei in the western United States in springtime and their relation to aerosol characteristics, J. Geophys. Res.-Atmos., 112, D02209, doi:10.1029/2006JD007500, 2007. 27303
Röckner, E., Brokopf, R., Esch, M., Giorgetta, M., Hagemann, S., Kornblueh, L., Manzini, E., Schlese, U., and Schulzweida, U.: Sensitivity of simulated climate to horizontal and vertical resolution in the ECHAM5 atmosphere model, J. Clim., 19, 3771–3791, 2006. 27289
Sander, R., Baumgaertner, A., Gromov, S., Harder, H., Joeckel, P., Kerkweg, A., Kubistin, D., Regelin, E., Riede, H., Sandu, A., Taraborrelli, D., Tost, H., and Xie, Z.: The atmospheric chemistry box model CAABA/MECCA-3.0, Geosci. Model Dev., 4, 373–380, doi:10.5194/gmd-4-373-2011, 2011. 27289
Sassen, K., DeMott, P. J., Prospero, J. M., and Poellot, M. R.: Saharan dust storms and indirect aerosol effects on clouds: CRYSTAL-FACE results, Geophys. Res. Lett., 30, 1633, doi:10.1029/2003GL017371, 2003. 27287
Shao, Y. and Raupach, M. R.: Effect of saltation bombardment on the entrainment of dust by wind, J. Geophys. Res.-Atmos., 98, 12719–12726, 1993. 27293
Sodemann, H., Palmer, A. S., Schwierz, C., Schwikowski, M., and Wernli, H.: The transport

ACPD
11, 27285–27325, 2011

history of two Saharan dust events archived in an Alpine ice core, Atmos. Chem. Phys., 6, 667–688, doi:10.5194/acp-6-667-2006, 2006. 27304

Stier, P., Feichter, J., Kinne, S., Kloster, S., Vignati, E., Wilson, J., Ganzeveld, L., Tegen, I., Werner, M., Balkanski, Y., Schulz, M., Boucher, O., Minikin, A., and Petzold, A.: The aerosol-climate model ECHAM5-HAM, Atmos. Chem. Phys., 5, 1125–1156, doi:10.5194/acp-5-1125-2005, 2005. 27290

Swap, R., Garstang, M., Greco, S., Talbot, R., and Kallberg, P.: Saharan dust in the Amazon Basin, Tellus B-Chem. Phys. Meteorol., 44, 133–149, 1992. 27287

Tegen, I., Harrison, S. P., Kohfeld, K., Prentice, I. C., Coe, M., and Heimann, M.: Impact of vegetation and preferential source areas on global dust aerosol: Results from a model study, J. Geophys. Res.-Atmos., 107, 4576, doi:10.1029/2001JD000963, 2002. 27286, 27288, 27290, 27291, 27292, 27298, 27304, 27305, 27313, 27315, 27316, 27317

Textor, C., Schulz, M., Guibert, S., Kinne, S., Balkanski, Y., Bauer, S., Berntsen, T., Berglen, T., Boucher, O., Chin, M., Dentener, F., Diehl, T., Easter, R., Feichter, H., Fillmore, D., Ghan, S., Ginoux, P., Gong, S., Kristjansson, J. E., Krol, M., Lauer, A., Lamarque, J. F., Liu, X., Montanaro, V., Myhre, G., Penner, J., Pitari, G., Reddy, S., Seland, O., Stier, P., Takemura, T., and Tie, X.: Analysis and quantification of the diversities of aerosol life cycles within AeroCom, Atmos. Chem. Phys., 6, 1777–1813, doi:10.5194/acp-6-1777-2006, 2006. 27287, 27294

Tost, H., Joeckel, P., Kerkweg, A., Sander, R., and Lelieveld, J.: Technical note: A new comprehensive SCAVenging submodel for global atmospheric chemistry modelling, Atmos. Chem. Phys., 6, 565–574, doi:10.5194/acp-6-565-2006, 2006. 27289

Vignati, E., Wilson, J., and Stier, P.: M7: An efficient size-resolved aerosol microphysics module for large-scale aerosol transport models, J. Geophys. Res.-Atmos., 109, D22202, doi:10.1029/2003JD004485, 2004. 27289

Washington, R., Todd, M., Middleton, N. J., and Goudie, A. S.: Dust-storm source areas determined by the total ozone monitoring spectrometer and surface observations, Ann. Assoc. Am. Geogr., 93, 297–313, 2003. 27294, 27295

Wernli, H. and Davies, H. C.: A Lagrangian-based analysis of extratropical cyclones .1. The method and some applications, Q. J. Roy. Meteorol. Soc., 123, 467–489, 1997. 27301

Zhao, T. L., Gong, S. L., Zhang, X. Y., and Jaffe, D. A.: Asian dust storm influence on North American ambient PM levels: observational evidence and controlling factors, Atmos. Chem. Phys., 8, 2717–2728, doi:10.5194/acp-8-2717-2008, 2008. 27298

ACPD
11, 27285–27325, 2011

Zuberi, B., Bertram, A. K., Cassa, C. A., Molina, L. T., and Molina, M.: Heterogeneous nucleation of ice in (NH4)(2)SO4-H2O particles with mineral dust immersions, Geophys. Res. Lett., 29, 1504, doi:10.1029/2001GL014289, 2002. 27287, 27303

ACPD
11, 27285–27325, 2011

Table 1. Input parameters for the dust emission schemes of Balkanski et al. (2004) and Tegen et al. (2002) for the Bodélé Depression and the Thar Desert.

Emission scheme	Parameter		Bodélé Depression	Thar Desert
Balkanski et al. (2004)	v_{thr}, m s^{-1}		7.2	6.0
	SSF		0.30×10^{-9}	1.08×10^{-9}
	LAI		0.00 in each month	0.43 in Jan to 0.27 in Jun, Jul, Aug
Tegen et al. (2002)	soil texture class	Coarse	1.00	0.14
		Coarse-medium	0.00	0.06
		Medium	0.00	0.26
		Medium-fine	0.00	0.55
		Fine	0.00	0.06

ACPD
11, 27285–27325, 2011

Table 2. Five-year mean values (2000–2004) of various dust parameters of the eight time slice simulations.

	Emission, Tg yr^{-1}	Load, Tg	Life time, d	Wet deposition, Tg yr^{-1}
T42BK	1651	27.85	6.19	1262
T63BK	2704	36.20	4.91	2096
T85BK	2841	31.50	4.09	2222
T106BK	3238	34.92	3.98	2557
T42TG	1683	26.63	5.85	1046
T63TG	1975	27.34	5.12	1174
T85TG	1815	22.18	4.55	1068
T106TG	2673	31.55	4.41	1588

ACPD
11, 27285–27325, 2011

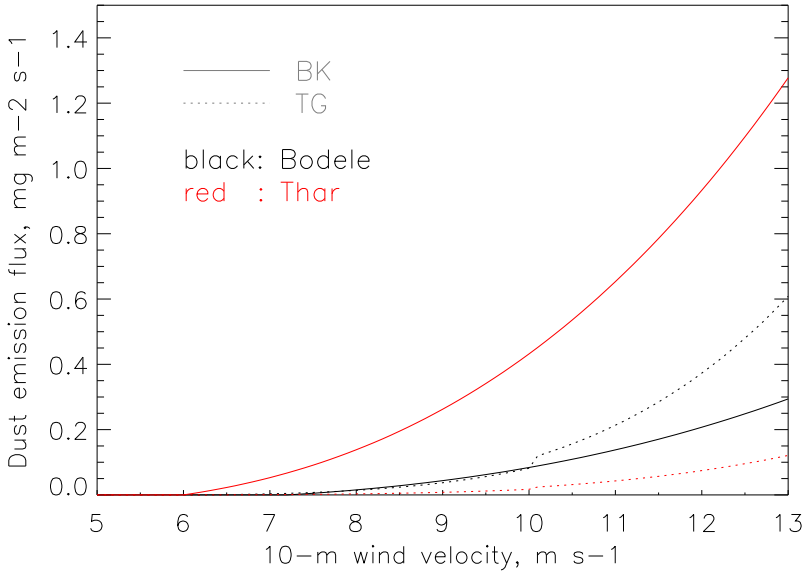

Fig. 1. Vertical dust emission flux (mg m^{-2} s^{-1}) vs. 10-m wind velocity (m s^{-1}) as simulated with the two dust emission schemes by Balkanski et al. (2004) (solid lines) and Tegen et al. (2002) in the Bodélé Depression (black) and the Thar Desert (red).

ACPD
11, 27285–27325, 2011

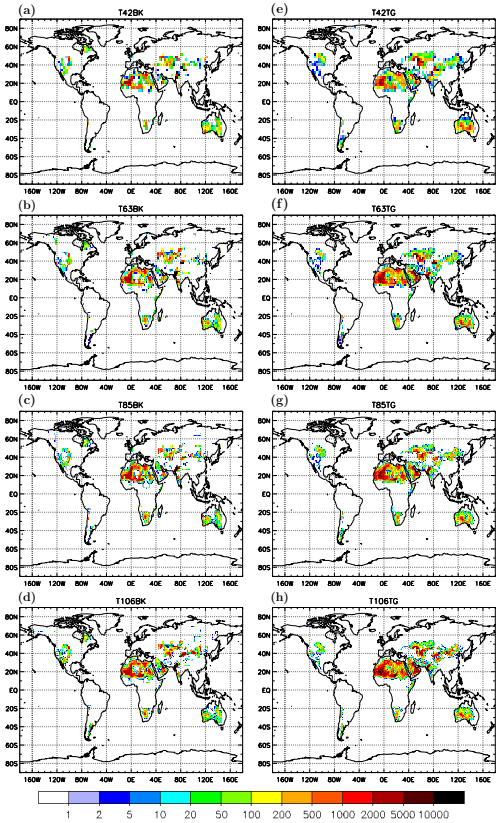

Fig. 2. Five-year mean dust emission (kg ha^{-1} yr^{-1}) of the simulations with the dust emission schemes of Balkanski et al. (2004) (left panels) and Tegen et al. (2002) (right panels) and for the spectral model resolutions T42 (1st row), T63 (2nd row), T85 (3rd row), and T106 (4th row).

ACPD
11, 27285–27325, 2011

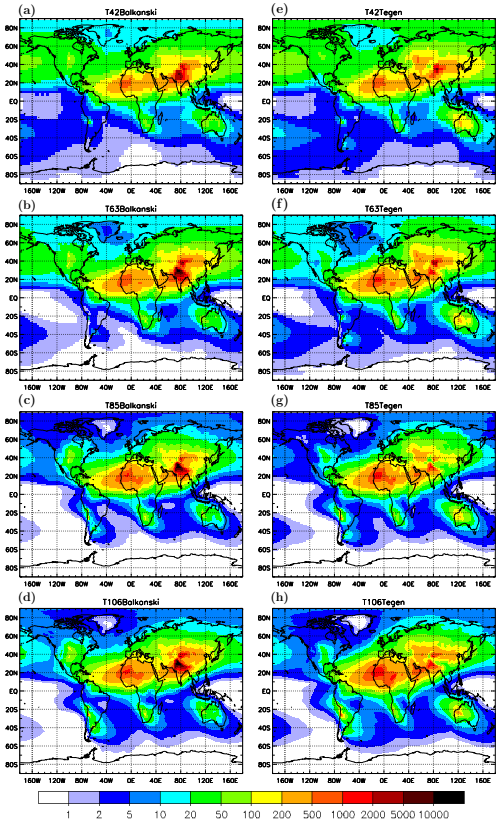

Fig. 3. Five-year mean dust column masses (mg m^{-2}) of the simulations with the dust emission schemes of Balkanski et al. (2004) (left panels) and Tegen et al. (2002) (right panels) and for the spectral model resolutions T42 (1st row), T63 (2nd row), T85 (3rd row), and T106 (4th row).

ACPD
11, 27285–27325, 2011

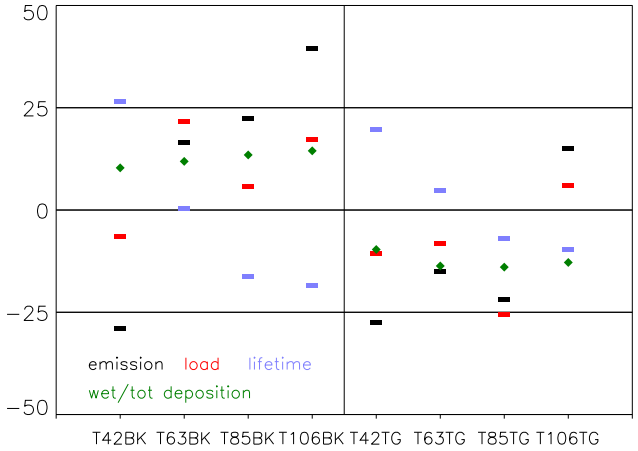

Fig. 4. Relative sensitivities of variables with respect to the model setup, according to Eq. (1).

ACPD
11, 27285–27325, 2011

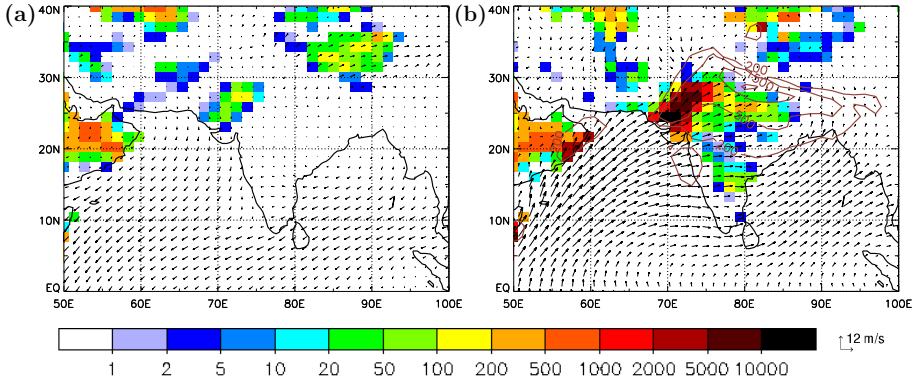

Fig. 5. Mean dust emission (kg ha^{-1}, shading), deposition (brown isolines for 200, 500, 1500, and 3000 kg ha^{-1}), and the wind on the lowest model layer (arrows) over the Indian subcontinent during DJF **(a)** and JJA **(b)** in the simulation T85TG.

ACPD
11, 27285–27325, 2011

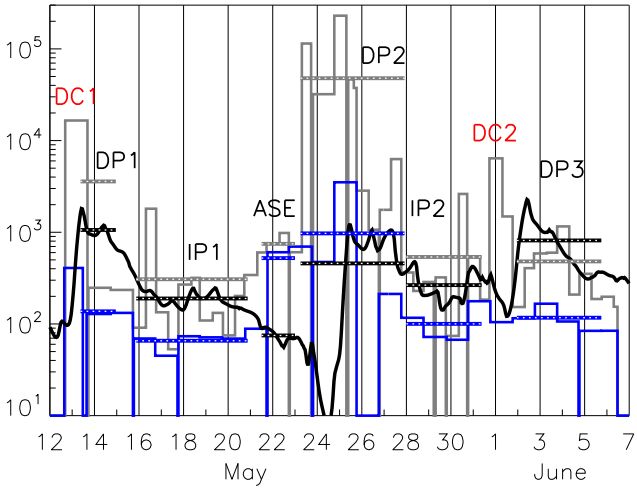

Fig. 6. Time series of the measured TSP (grey) and PM_{10} (blue) concentrations at Tinfou, Morocco and the simulated dust concentrations in the grid box containing Tinfou with T85TG ($\mu g\,m^{-3}$). Horizontal bars with white dottet lines on it show the mean values for the periods defined by Kandler et al. (2009), DC1 and DC2 mark the two density currents, observed during SAMUM.

ACPD
11, 27285–27325, 2011

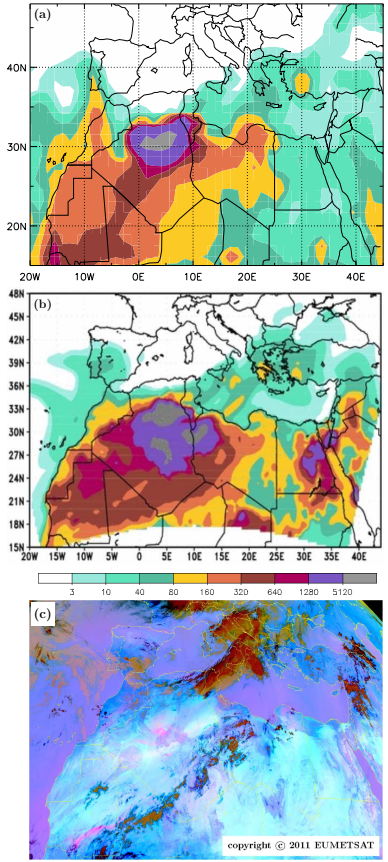

Fig. 7. Dust concentration (μg m^{-3}) on the lowest model layer of EMAC **(a)** and BSC/DREAM8b **(b)**, respectively and MSG dust RGB composite **(c)** on 1 June 2006 12:00 UTC.

ACPD
11, 27285–27325, 2011

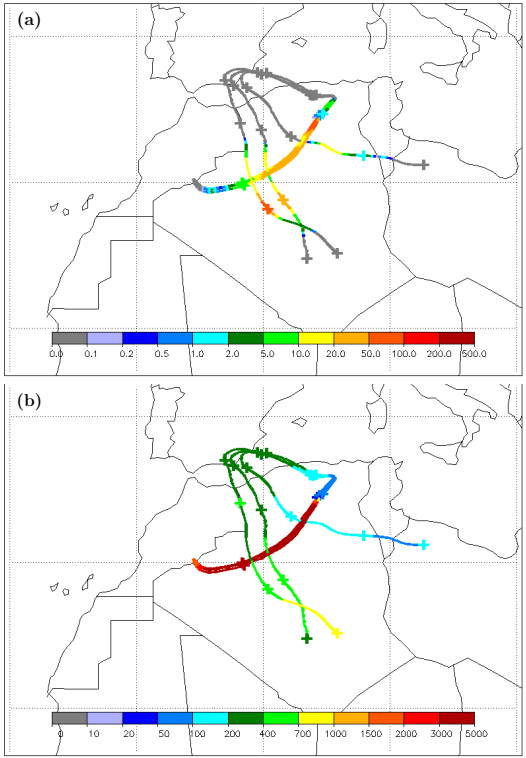

Fig. 8. Eight-day backward trajectories initialised on 3 June 2006 00:00 UTC starting from the three lowest model layers at Tinfou. A "+" is drawn every 24 h. Coloured variables along the trajectories are **(a)** the dust emission ($\mu g\,m^{-2}\,s^{-1}$) and **(b)** the dust concentration ($\mu g\,m^{-3}$).

ACPD
11, 27285–27325, 2011

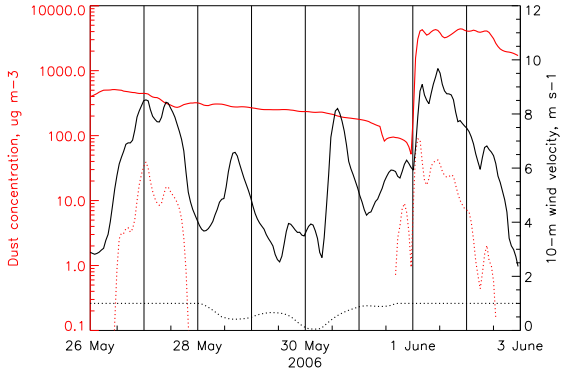

Fig. 9. Mean values along the trajectories. According to the left axis: dust concentration (solid red line, $\mu g\,m^{-3}$), dust emission (dotted red line, $\mu g\,m^{-2}\,s^{-1}$); according to the right axis: 10-m wind velocity (solid black line, $m\,s^{-1}$), Land-Sea-Mask (dotted black line).

ACPD
11, 27285–27325, 2011

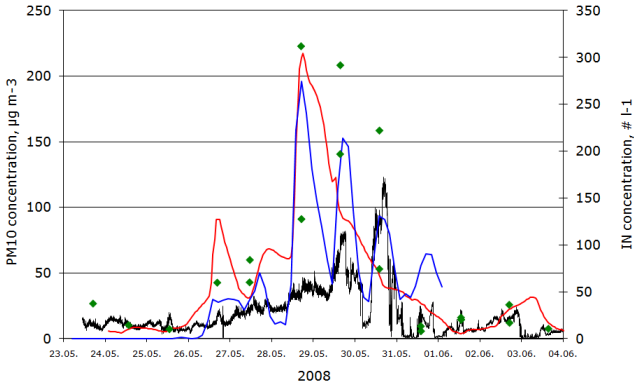

Fig. 10. According to the left axis: time series of the measured PM_{10} concentration (black line, $\mu g\,m^{-3}$) at Mt. Kleiner Feldberg, Germany and the simulated dust concentrations at Mt. Kleiner Feldberg of EMAC (red line) and BSC/DREAM8b (blue line). According to the right axis: measured number concentration of ice nuclei (green diamonds, # l^{-1}). Measurements are described in Klein et al. (2010).

ACPD
11, 27285–27325, 2011

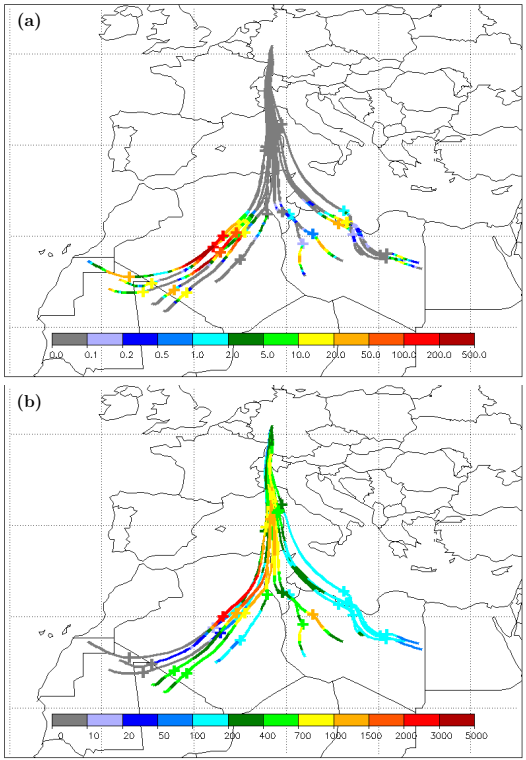

Fig. 11. 90-h backward trajectories initialised on 28 May 2008 18:00 UTC starting in intervals of 30 hPa from the surface to 350 hPa at Mt. Kleiner Feldberg. Only trajectories with northward displacement larger than 22° latitude are displayed. Coloured variables along the trajectories are **(a)** the dust emission ($\mu g\,m^{-2}\,s^{-1}$) and **(b)** the dust concentration ($\mu g\,m^{-3}$). A "+" is drawn every 24 h.

ACPD
11, 27285–27325, 2011